Temperature and isospin dependence of the level-density parameter in the $A \approx 110$ mass region

G. K. Prajapati,[1,*] Y. K. Gupta,[1,2] B. V. John,[1,2] B. N. Joshi,[1] Harjeet Kaur,[3] Nishant Kumar,[1,2] L. S. Danu,[1] S. Mukhopadhyay,[1] S. Dubey,[1,4,†] S. R. Jain,[1] D. C. Biswas,[1] and B. K. Nayak[1]

[1]*Nuclear Physics Division, Bhabha Atomic Research Centre, Mumbai 400085, India*

[2]*Homi Bhabha National Institute, Mumbai 400094, India*

[3]*Guru Nanak Dev University, Amritsar 143005, India*

[4]*Physics Department, Faculty of Science, M.S. University of Baroda, Vadodara 390002, India*

(Received 20 March 2020; revised 1 September 2020; accepted 6 October 2020; published 9 November 2020)

α-Particle evaporation spectra were measured at backward angles in $^{16}O + {}^{94,100}Mo$ reactions at multiple beam energies. Inverse level-density parameter, K, was determined for Cd nuclei of different isospins by simulating high-energy tail of the measured α-particle evaporation spectra with statistical model code PACE2. An overall increasing behavior of the K value is observed with increasing temperature in the range of 1 to 2.5 MeV. It is observed that in the temperature region below 1.8 MeV, the parameter K is higher for the neutron-rich nuclei by around 1 MeV. Semiclassical calculations were performed which treat single-particle level density of neutron and proton on different footing and this can account for the isospin effects. These calculations reproduce the K values as determined from the statistical model analysis of α-particle evaporation spectra. Present results clearly demonstrate the isospin dependence of the level-density parameter as conjectured by theoretical works.

DOI: 10.1103/PhysRevC.102.054605

I. INTRODUCTION

Nuclear level-density (NLD) is a fundamental property of atomic nucleus and plays a crucial role to understand several physical phenomena in nuclear physics and astrophysics. It is a key ingredient in the prediction of nuclear reaction cross sections using statistical models. Therefore, it is also a very important input parameter in designing new nuclear technologies. It is often necessary to have an accurate estimate of the NLD of highly excited nuclei as a function of the excitation energy, angular momentum, isospin, and other constants of motion. Primarily, it is described in a phenomenological framework, where its excitation energy dependence is given by the Fermi-gas (FG) approximation [1] as

$$\rho(E_X) = \frac{\sqrt{\pi}}{12} \frac{\exp(2\sqrt{aE_X})}{a^{1/4} E_X^{5/4}}, \tag{1}$$

where E_X is the excitation energy of the nucleus and a is the nuclear level-density parameter, which is related to the single-particle level-density $g(\varepsilon_F)$ at the Fermi energy (ε_F) through the relation $a = (\pi^2/6)g(\varepsilon_F)$. Influence of other important factors on the level-density parameter, such as, shell effects, pairing, collectivity, etc., are taken into account through a number of adjustable parameters [2–4]. It is more convenient to use the inverse level-density parameter, $K = A/a$, where A is the mass number of the nucleus. In the FG approximation, the parameter K is constant around 15 MeV. At excitation energies around the particle emission threshold, the inverse level-density parameter, K, exhibits a dramatic variation around the shell closures due to prominent shell effects. However, an average trend of $K = 8$–9 MeV is observed while spanning almost the whole nuclear chart. With increasing excitation energies, the shell effects are depleted, and the parameter K approaches to its asymptotic value at nuclear temperatures, $T > 1$ MeV, and this aspect is understood well [5].

Initially, it was a puzzle that the average magnitude of the NLD parameter, a, is around $A/8$ MeV^{-1}, which is significantly higher than the FG value of $A/15$ MeV^{-1}. With increasing excitation energies, however, it is observed that the level-density parameter approaches to the FG value of $A/15$ MeV^{-1} [6–13]. Febris *et al*. [10] has shown from evaporated α-particle spectra in $^{19}F + {}^{181}Ta$ reaction that K values increase from 8 to 14 MeV while scanning the beam energy from 90 to 140 MeV. Similarly, Roy *et al*. [14] has reported from evaporated neutron spectra in mass region around $A = 210$ that K values increase from 7.8 to 10 MeV with increase in temperature from 0.7 to 1.4 MeV. The intriguing variation of $K \simeq 8$ MeV from low temperature to the FG value of $K \simeq 15$ MeV at $T \approx 5$ MeV has been attributed to the effects arising from finite nuclear size and effective nucleonic mass [8,15,16]. Calculations by Shlomo and Natowitz [8,16] which include finite nuclear size, effective nucleonic mass, and shell effects support the experimental trend of increasing K value with temperature. However, these predict quite different rates of increase in K with temperature in different regions of the nuclear chart. As the nuclear level-density parameter is directly related to microscopic aspects of the atomic nucleus, its temperature dependence is of fundamental importance.

*shyam@barc.gov.in

†Present address: Tata Institute of Fundamental Research, Mumbai 400005, India.

Temperature dependence of the NLD parameter also plays a key role in constraining caloric curves which further determine the phase transition in finite nuclear matter [17–19]. As suggested by the theory [8,16], it is of utmost importance to obtain experimental value of the parameter K with varying temperature in different mass regions.

Similarly to the temperature dependence of the single-particle level densities, the isospin effects are not included within the Fermi-gas framework. The isospin is expected to influence two quantities: the level-density parameter a and the symmetry energy contribution to the nuclear masses [20,21]. It has been conjectured in Ref. [22] that in contrast to Fermi-gas framework, the parameter a actually depends on N and Z separately, where N and Z refer to the numbers of neutrons and protons, respectively. This is justified when proton and neutron single-particle level densities are unequal. According to Quraishi *et al*. [22,23], the NLD parameter a is reduced as one moves away from the valley of stability. Calculations based on relativistic mean-field theory [24] have also demonstrated the isospin dependence of the parameter a. The variation of the NLD parameter with isospin is of significant importance for *r*- and *rp*-processes in nuclear astrophysics where the synthesized nuclei are considerably proton or neutron rich. A clear understanding of isospin dependence of the NLD parameter a is crucial not only because of its vital role in the nuclear synthesis but also for the microscopic understanding of different effects arising as one moves away from the valley of stability.

Recently, Kaur and Jain [25] have also proposed a semiclassical theory of the shell effect melting in nuclei with temperature using an exact semiclassical trace formula. This formula allows us to treat single-particle level density of neutron and proton on different footing, and this can account for the isospin effects. Moreover, it can calculate single-particle level densities for spherical and axially symmetric harmonic oscillator potentials, thereby accounting for the deformation effects. In order to benchmark the semiclassical theory of Kaur and Jain [25], experimental data on simultaneously varying temperature and isospin are needed.

On the experimental front, the information about the isospin dependence of the nuclear level-density parameter using stable beams is very sporadic [6,26], primarily because of mild effects for nuclei close to the valley of stability. With the development of RIB facilities, there is a renewed interest in investigating the isospin effects on single-particle nuclear-level densities in the vicinity of drip lines [27]. However, the disadvantage with radioactive beams lies with their poor intensities. It is therefore of primary importance to test the effect of the isospin on level densities by forming compound systems as exotic as possible using stable ion beams.

Experimental information about the nuclear level-density parameter a at excitation energies well above the neutron separation and below 5 MeV/nucleon can be obtained from the high-energy slope of evaporated particle spectra from heavy-ion fusion reactions [3,28–34]. In order to study the temperature dependence of NLD parameter and to search for any evidence of isospin dependence, we have measured the α-particle evaporation spectra from ^{110}Sn* and ^{116}Sn* compound nuclei populated in ^{16}O + ^{94,100}Mo reactions at several excitation energies. Inverse level-density parameter, K, as a function of temperature, T, has been determined by fitting the experimental α-particle spectra measured at backward angles with simulated spectra using the statistical model code PACE2 [35]. In this paper, we present detailed data analysis and results on temperature and isospin dependence of the nuclear level-density parameter. The paper is organized as follows. The experimental details of the measurements have been discussed in Sec. II. Section III describes data analysis and statistical model calculations using the code PACE2. Results and discussion are presented in Sec. IV. Section V contains semiclassical calculation of NLD using Ref. [25] and a comparison thereof for the Cd isotopes, populated in the present reactions. The present work is summarized in Sec. VI.

II. EXPERIMENTAL DETAILS

The experiment was carried out using ^{16}O beam from BARC-TIFR Pelletron Linac Accelerator Facility at Mumbai. ^{16}O beam of varying energies bombarded isotopically enriched (>95%) and self-supporting foils of ^{94}Mo and ^{100}Mo with thicknesses of 1.8 mg/cm^2 and 1.0 mg/cm^2, respectively. α-Particle evaporation spectra in the ^{16}O + ^{94}Mo reaction were measured at five different beam energies of 55, 60, 70, 75, and 80 MeV. In the case of the ^{16}O + ^{100}Mo reaction, 10 beam energies (55, 60, 70, 75, 80, 95.5, 104.9, 114.6, 124.6, and 136.6 MeV) were used. The beam energies were corrected for energy loss in the half-thickness of the target. α-Particles were detected using CsI(Tl) detectors of dimension 2.5 cm × 2.5 cm × 1.0 cm coupled to Si(PIN) photodiodes [36,37]. These detectors were mounted in the backward hemisphere of the Charge Particle Detector Array [38] at a distance of 17 cm from the target at angles of 115°, 125°, 130°, 134°, 140°, 145°, 150°, and 155° with respect to the beam direction. Two silicon surface barrier detectors having solid angle of ≈0.027 msr were placed at ±20° at both sides of the beam direction for the Rutherford normalization purpose. The CsI(Tl) detectors were energy calibrated in the range of 4.8 to 8.4 MeV using ^{228,229}Th α-source periodically throughout the experiment duration. Extrapolation of the light yield produced in the CsI(Tl) detectors beyond 8.4 MeV was estimated using in-beam data from earlier measurements [39,40]. Particle identification in the CsI(Tl) detectors was achieved using the "ballistic deficit" technique [41]. It required two different shaping time amplifiers, one with a short shaping time (0.2 μs) and another with a long shaping time (3.0 μs). The correlation between long (PH$^{\mathrm{Long}}$) versus short (PH$^{\mathrm{Short}}$) integration pulse heights resulted in different bands for different particles [42] as shown in Fig. 1 for ^{16}O (136.6 MeV) + ^{100}Mo reaction at a laboratory angle of 150°. The particle identification (PID) parameter was generated using the following equation;

$$\mathrm{PID} = \frac{\mathrm{PH}^{\mathrm{Long}} - \mathrm{PH}^{\mathrm{Short}}}{\mathrm{PH}^{\mathrm{Long}}}. \tag{2}$$

A two-dimensional plot of PID versus PH$^{\mathrm{Long}}$ corresponding to the plot depicted in the Fig. 1 is shown in Fig. 2. Different bands corresponding to γ rays, $Z = 1$, $Z = 2$, PLF, and PIN-γ rays are clearly separated in Fig. 2, where PLF and PIN-γ

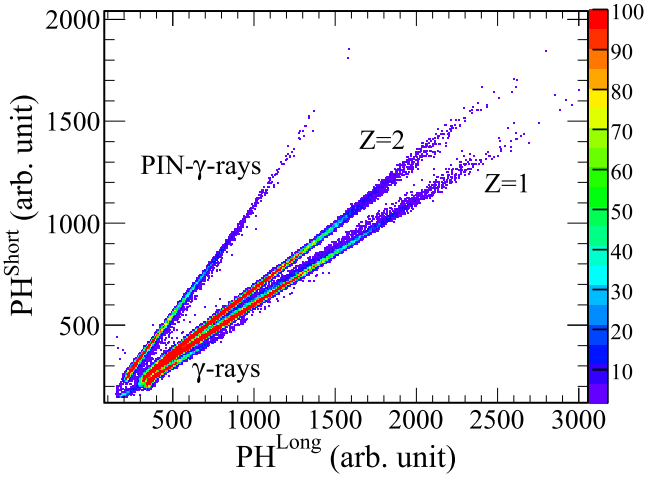

FIG. 1. Two-dimensional plot of short shaping time pulse heights versus long shaping time pulse height for ^{16}O (136.6 MeV) + ^{100}Mo reaction at a laboratory angle of $\theta_{lab} = 150^{\circ}$.

rays refer to the projectile like fragments and γ rays reaching directly to the photodiode of the CsI(Tl) detector [36], respectively. The $Z = 2$ band corresponds most dominantly to the α particles, and it is enclosed using a red solid line in the Fig. 2.

III. DATA ANALYSIS

The α-particle yield spectra were extracted out from the PID versus PH^{Long} plots ($Z = 2$ band) for different angles. The α-particle yields were converted to double differential cross sections, $d^2\sigma/d\Omega dE$, by normalizing with the Rutherford scattering events from the monitor detector placed at an angle of 20° with respect to the beam direction. The α-particles energy spectra, thus obtained at different laboratory angles were converted to the center-of-mass frame using standard Jacobian transformation. The center-of-mass spectra of different laboratory angles overlapped well with each other within the experimental uncertainties as shown in Fig. 3 for the ^{16}O + ^{100}Mo reaction at one typical beam energy of 136.6 MeV. Similarly to the ^{16}O + ^{100}Mo reaction, the center-of-mass spectra of different laboratory angles for the ^{16}O + ^{94}Mo reaction overlapped with one another as well. The error bars on the data points included only the statistical uncertainties. Overlapping of the center-of-mass spectra of different laboratory angles establishes that the dominant yield of α particles is from the compound nucleus evaporation. The center-of-mass energy spectra of different laboratory angles were averaged at each beam energy for both the systems. Averaged α-particle energy spectra from the ^{16}O (80 MeV) + ^{94}Mo and ^{16}O (70 MeV) + ^{100}Mo fusion reactions, populating compound nuclei, ^{110}Sn* and ^{116}Sn*, respectively, at similar excitation energy of 59.5 MeV (after correcting for the energy loss in the targets), are shown in the Fig. 4. It has been observed that at similar excitation energy, the overall yield of α particles in ^{16}O + ^{94}Mo reaction is close to five times to that of the ^{16}O + ^{100}Mo reaction which might be attributed to the differences in the particle separation energies as discussed later. The averaged center-of-mass spectra from the decay of compound nuclei, ^{110}Sn* and ^{116}Sn* at different beam energies are shown in Figs. 5 and 6, respectively. The energy spectra at different beam energies were scaled by suitable factors in Figs. 5 and 6 for better visualization. The solid histograms in Figs. 5

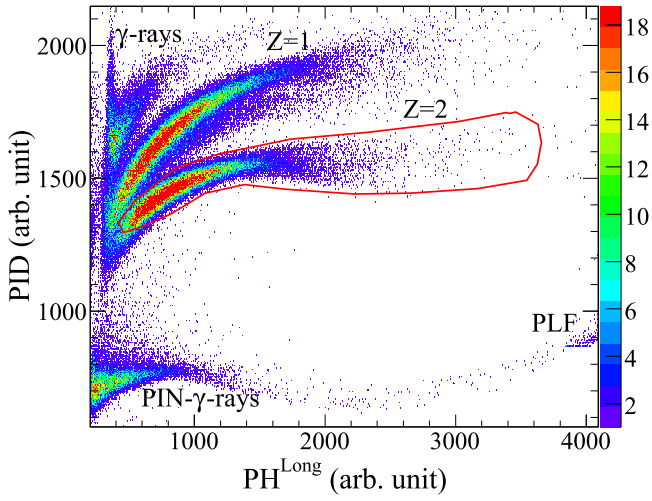

FIG. 2. Two-dimensional plot of PID versus pulse height (long shaping time) for ^{16}O (136.6 MeV)+ ^{100}Mo reaction at a laboratory angle of $\theta_{lab} = 150^{\circ}$.

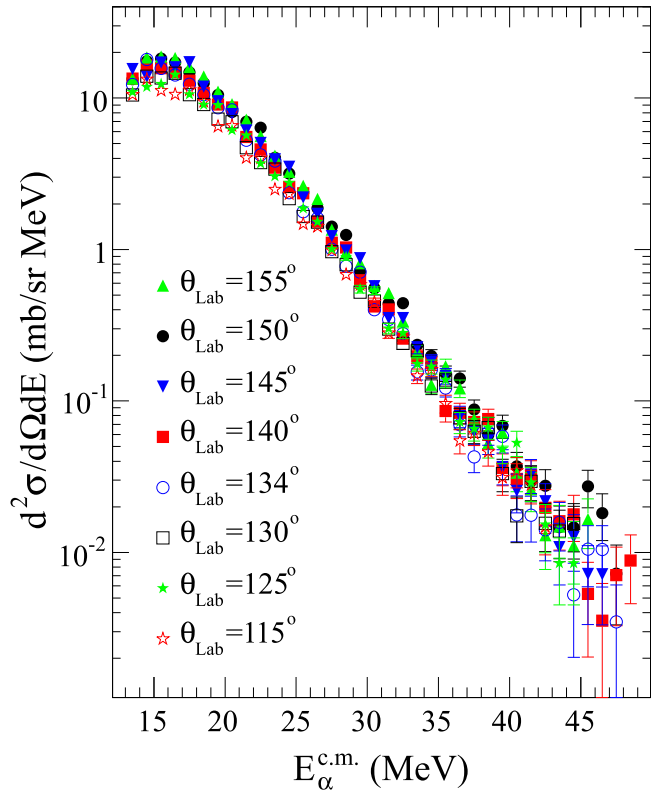

FIG. 3. α-particle energy spectra in center-of-mass frame at different laboratory angles for ^{16}O + ^{100}Mo reaction at a beam energy of 136.6 MeV.

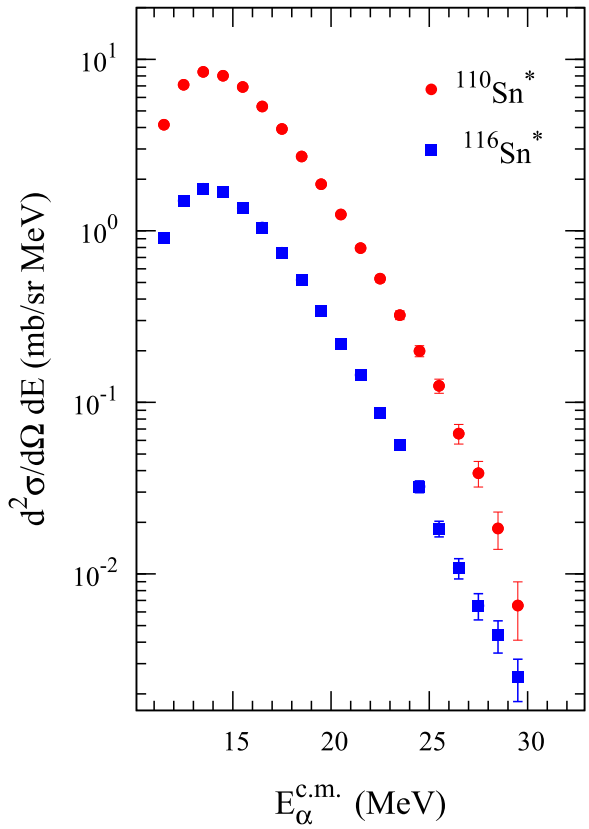

FIG. 4. Measured α-particle energy spectra from ^{16}O (80 MeV) + ^{94}Mo and ^{16}O (70 MeV) + ^{100}Mo fusion reactions, populating compound nuclei, ^{110}Sn* and ^{116}Sn*, respectively at similar excitation energy of 59.5 MeV (see text).

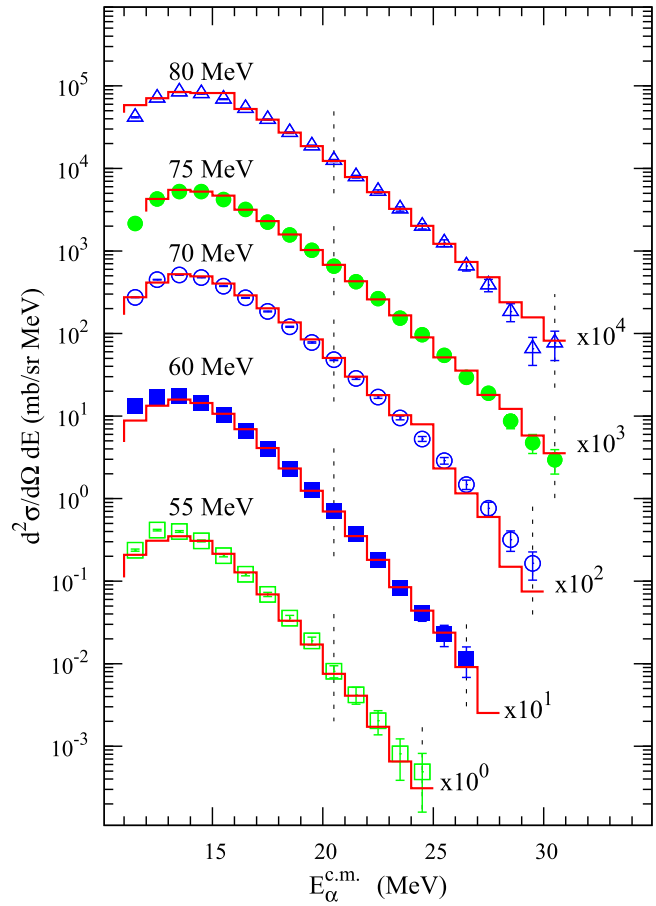

FIG. 5. Averaged α-particle energy spectra in center-of-mass system (symbols) at different beam energies for ^{16}O + ^{94}Mo reaction. Solid histograms represent the best fit statistical model calculations (using PACE2 code). The individual spectrum has been scaled for a better visualization. The beam energies and scaling factors are mentioned along with each curve. The two vertical lines along each curve show the kinetic energy region chosen for the χ^2 minimization (see text).

and 6 representing the statistical model calculations will be elaborated later in the text.

Averaged center-of-mass energy spectra at each beam energy were compared with the statistical model prediction using the Monte Carlo code PACE2 [35]. Compound nucleus spin distribution used in the code PACE2 is given by

$$\sigma_J = \pi\lambda\!\!\!^{-2}\frac{(2J+1)}{[1+\exp\{(J-J_{\rm crit})/\Delta\}]}, \qquad (3)$$

where σ_J is the compound nuclear partial cross section for the spin J and $\lambda\!\!\!^{-}$ is the reduced wave length. In Eq. (3), Δ is the diffuseness parameter and $J_{\rm crit}$ is the critical angular momentum for the fusion process. $J_{\rm crit}$ is estimated by the total fusion cross section, σ_F ($\sigma_F = \sum\sigma_J$). PACE2 code takes ground-state spins of projectile and target into account, and, accordingly, Δ was chosen to be $0.3\hbar$. PACE2 code calculates the total fusion cross section from Bass systematics [43]. Energy and angular momentum-dependent level-density $\rho(E_X, J)$ that is used in the PACE2 calculations for an excitation energy (E_X) above 5 MeV is given by

$$\rho(E_X, J) = \frac{2J+1}{12}\sqrt{a}\left(\frac{\hbar}{2I}\right)^{3/2}\frac{\exp(2\sqrt{aU})}{U_{\rm ex}^2}, \qquad (4)$$

where $U_{\rm ex} = E_X - \Delta P(Z) - \Delta P(N)$ and $U = U_{\rm ex} - E_{\rm rot}$, where $E_{\rm rot} = \frac{\hbar^2}{2I}J(J+1)$ is the rotational energy. U is the net thermal energy available for nuclear excitation. $\Delta P(Z)$ and $\Delta P(N)$ are the pairing energy differences obtained from Gilbert and Cameron's compilation for odd-even mass differences of the nuclear ground state. The moment of inertia I was calculated using Sierk rotating liquid drop model [44]. We employed Ignatyuk's prescription [5] which is widely used in phenomenological descriptions of nuclear level-density as it takes into account the variation of the level-density parameter a in the vicinity of shell closures;

$$a = \tilde{a}\left\{1 - \frac{\Delta S}{U}[\,1 - \exp(-\gamma U)\,]\right\}, \qquad (5)$$

where $\tilde{a}$ is the asymptotic value of the level-density parameter and γ is the shell damping factor for which we have used the value of 0.054 MeV^{-1}. The shell correction factor ΔS was calculated using the Swiatecki and Myers formalism [45], with the convention of being +ve for the closed shell nuclei. The transmission coefficient as a function of energy and orbital angular momentum of the emitted particle is con-

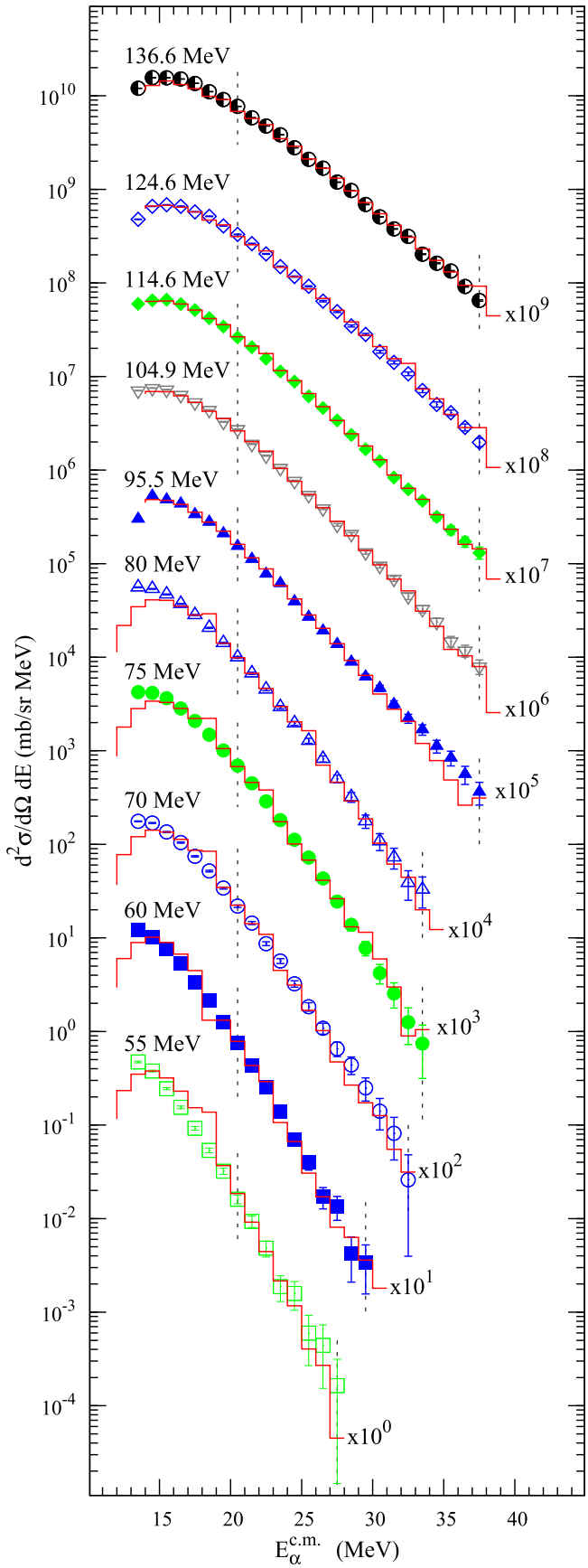

FIG. 6. Same as in Fig. 5 but for the $^{16}O + {}^{100}Mo$ reaction.

ventionally generated by the optical model potentials (OMPs). In the present calculations for α-particle emission, the OMP parameters of Igo and Huizenga [46] were used. In the present work the primary aim is to study the level-density parameter from the shape of the evaporated α-particle spectra with varying excitation energy. The high-energy tail of the spectrum (well above the emission barrier) is dominantly decided by the variation of nuclear level densities in the residual nuclei with energy available. The transmission coefficients, and hence, the OMP parameters influence the α-particle spectrum around and below the emission barrier. Therefore, the choice of OMP parameters does not affect the investigation of the level-density parameter.

In order to estimate the roles of first and higher chances of α-particle emission in determining the relevant residual nuclei for which the present analysis is valid for, the following exercise was carried out. PACE2 calculations were carried out for $^{16}O + {}^{94}Mo$ and $^{16}O + {}^{100}Mo$ fusion reactions such that both the compound nuclei are populated with the same initial excitation energy of 60 MeV. The asymptotic value of the level-density parameter was chosen to be $A/10$ MeV^{-1} for both the reactions. Using the traceback feature of the code PACE2, the fraction of α-particle emission from different stages, such as, first chance (0n), after one neutron emission (1n), and after two neutron emission (2n), were estimated. Figure 7 shows PACE2 calculated α-particle spectra of different emission stages as well as the inclusive ones for both the reactions. The PACE2 simulated inclusive multiplicities for neutron, proton, and α particle are seen to be 2.12, 1.11, and 0.38 for the $^{16}O + {}^{94}Mo$ reaction and 3.72, 0.25, and 0.08 for the $^{16}O + {}^{100}Mo$ reaction, respectively. The difference in the particle multiplicities is attributed to the difference in the particle separation energies. The separation energies for neutron (S_n), proton (S_p), and α-particle (S_α) emissions from the populated $^{110}Sn^*$ compound nucleus are 11.282, 6.643, and 1.135 MeV, and from the $^{116}Sn^*$ compound nucleus, these values are 9.563, 9.278, and 3.375 MeV, respectively. The 0n and 1n contributions relative to the inclusive spectrum in the kinetic energy range of α particles beyond 20 MeV are seen to be, respectively, 60% and 30.3% for the $^{16}O + {}^{94}Mo$ reaction and 35.6% and 62.6% for the $^{16}O + {}^{100}Mo$ reaction. The first chance α-particle emission from the $^{110}Sn^*$ compound nucleus is much more than the $^{116}Sn^*$ compound nucleus in the kinetic energy range beyond 20 MeV which is consistent with the more favorable neutron separation energy in case of $^{116}Sn^*$. Despite these differences in separation energies and hence the particle multiplicities, the shapes of 0n+1n and inclusive α-particle spectra from both the reactions are similar in the higher kinetic energy region (> 20 MeV), as seen from Figs. 7(c) and 7(d) where the spectrum from the $^{116}Sn^*$ compound nucleus has been scaled up by a factor 7.8. It is concluded from PACE2 predictions that the emission of higher kinetic energy (>20 MeV) α particles predominantly takes places as the first chance or followed by one neutron emission for both the reactions. The fraction of 0n+1n events of α-particle emission in the higher kinetic energy region (>20 MeV) where shape of the spectrum is predominantly decided of the energy-dependent nuclear level densities, is more than 90% for both the reactions.

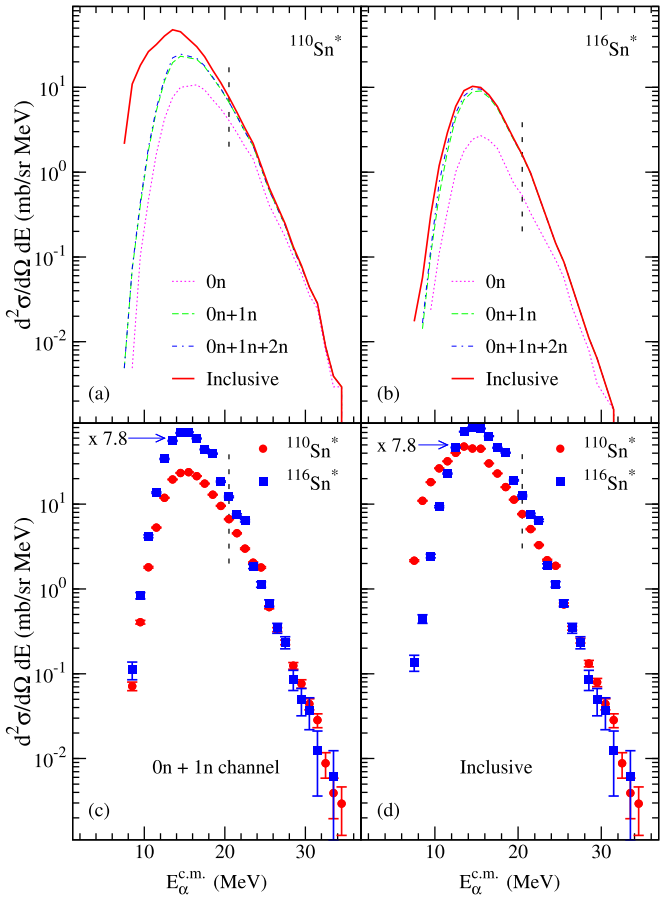

FIG. 7. PACE2 predicted α-particle energy spectra from ^{16}O (78.78 MeV) + ^{94}Mo and ^{16}O (68.91 MeV) + ^{100}Mo fusion reactions, populating compound nuclei, ^{110}Sn* and ^{116}Sn*, respectively, at same excitation energy of 60 MeV, and with inverse level-density parameter, $K = 10$ MeV. α-particle emission spectra from different stages, such as, first chance (0n), after one neutron emission (1n), after two neutron emission (2n), and inclusive (all channels) are determined. The dotted vertical lines in each panel mark the position of 20-MeV α-particle kinetic energy. (a) Contributions from 0n, 0n+1n, 0n+1n+2n, and inclusive for compound nucleus ^{110}Sn* are shown by dotted (magenta), dashed (green), dash-dotted (blue), and solid (red) lines, respectively. (b) Same as panel (a) but for the ^{116}Sn* compound nucleus. (c) 0n+1n channels are compared for compound nuclei ^{110}Sn* (red solid circles) and ^{116}Sn* (blue solid squares) where contribution for ^{116}Sn* is scaled up by a factor of 7.8. (d) Same as panel (c), but for inclusive contribution. In panels (c) and (d), uncertainties correspond to statistical fluctuation in the Monte Carlo simulation of PACE2.

Averaged center-of-mass α-particle spectrum at each beam energy was compared with corresponding PACE2 prediction for both ^{16}O + ^{94}Mo and ^{16}O + ^{100}Mo reactions. The inverse level-density parameter $K = A/\tilde{a}$ was kept as free parameter to obtain the best fit using χ^2 minimization technique. The χ^2 minimization was performed in the kinetic energy region beyond 20 MeV as marked by two vertical lines in the Figs. 5 and 6.

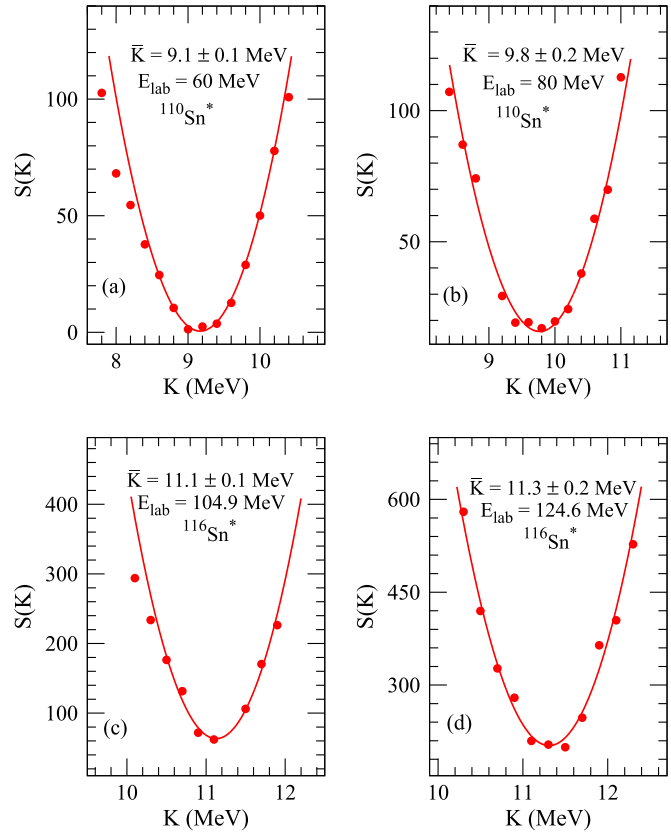

FIG. 8. Parabolic variation of $S(K)$ with parameter K for some typical cases for compound nuclei ^{110}Sn* and ^{116}Sn*.

The most probable value of K is obtained by minimizing the statistical variance given by [33,34]:

$$S(K) = \sum_{i=1}^{N} \frac{[Y_i - f_i(K)]^2}{\sigma_i^2}, \tag{6}$$

where Y_i, is the double differential cross section in ith energy bin, $f_i(K)$ is the results of calculation from PACE2 code for the same energy bin for the inverse level-density parameter K, and σ_i^2 is the statistical error in measured cross section. If the functional form of $f_i(K)$ is correct and the errors, σ_i, in Y_i are normally distributed, then the minimum $S(\bar{K})$ obey the chi-square $\chi^2(N-1)$ distribution with $N-1$ degrees of freedom, where N is the number of data points considered. We have determined the $S(K)$ as a function of K using the above equation and in most cases a parabolic dependence of $S(K)$ on K is observed as shown in Fig. 8 for some typical cases. The best fit parameter $\bar{K}$ was determined from the minimum of the parabola. To define error δK on $\bar{K}$, an interval of 68.3% confidence level was determined (corresponding to one standard deviation) using a limit on $S(K)$ defined as [47]:

$$S_L = S(\bar{K}) + \frac{S(\bar{K})}{N-1}. \tag{7}$$

The error δK is defined as the intercept of the parabola with the limit S_L. Thus, best-fitted inverse level-density parameter

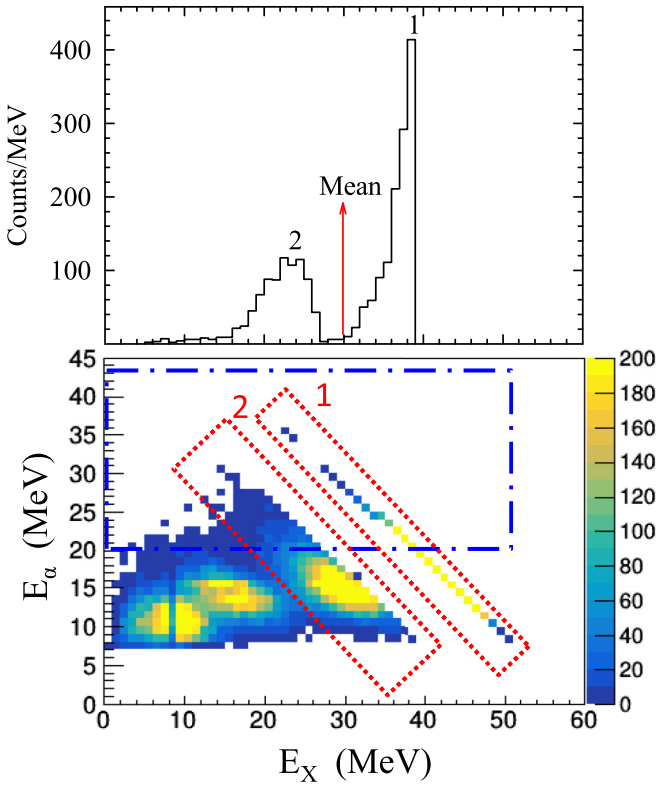

FIG. 9. Bottom panel: Two-dimensional plot of α-particle kinetic energy versus residual nuclei excitation energy as obtained from PACE2 calculations (using K=10 MeV) for ^{116}Sn* compound nucleus with initial excitation energy of 60 MeV. Two enclosed rectangular boxes (dotted, red-color), named as "1" and "2," respectively refer to the first chance and second chance α-particle emissions. The another rectangular box (blue, dash-dotted) marks the α-particle events with kinetic energy (E_α) more than 20 MeV. Top panel: Projection of the bottom-panel two-dimensional plot on the residual nuclei excitation energy axis for $E_\alpha > 20$ MeV (see text).

$\bar{K}$ is obtained as a function of beam energy for both the reactions.

Selected α-particle kinetic energy range corresponds to a range of excitation energy in the residual nuclei. As discussed earlier, for the present reactions, both 0n and 1n channels contribute to the α-particle kinetic energy beyond 20 MeV, for which χ^2 minimization is performed to get the best fit inverse level-density parameter. In order to determine an average excitation energy of the residual nuclei after α-particle emission, the trace-back feature of PACE2 was employed using the most probable $\bar{K}$ value for each beam energy. At first, a two-dimensional plot of α-particle kinetic energy versus excitation energy in the residual nuclei was obtained. A typical two-dimensional plot is shown in the bottom panel of Fig. 9 for ^{16}O + ^{94}Mo reaction for an initial excitation energy of 60 MeV and K = 10 MeV. In the bottom panel of Fig. 9, the two enclosed rectangular boxes (dotted, red-color), named as "1" and "2," respectively refer to the first chance and second chance α-particle emissions. Another rectangular box (blue, dash-dotted) marks the α-particle events with kinetic energy more than 20 MeV. In the top panel of Fig. 9, projection of the two-dimensional plot on the residual nuclei excitation energy axis for $E_\alpha > 20$ MeV is shown, where, the peaks, named as "1" and "2," respectively refer to the first chance and second chance α-particle emissions. The arrow indicates the mean excitation energy ($\bar{E}_X$ = 23.8 MeV) of the residual nuclei. This procedure was followed for each beam energy used for both the systems. The $\bar{E}_X$ values thus determined corresponding to each beam energy are listed in Table I.

The $\bar{E}_X$ value was subsequently converted to nuclear temperature (T) using following equation from Ref. [48]:

$$\frac{1}{T} = -\frac{5}{4\bar{E}_X} + \sqrt{\frac{\tilde{a}}{\bar{E}_X}}, \tag{8}$$

where $\tilde{a} = A/8$ MeV^{-1} was chosen. Here, A = 106 and 112 have been used for the two systems respectively, as an approximation.

IV. RESULTS AND DISCUSSIONS

Experimental α-particle energy spectra along with the best fit PACE2 calculations (using $\bar{K}$) are given in Figs. 5 and 6 for both the compound nuclear systems at different beam energies. The best fit inverse level-density parameters, $\bar{K}$ and temperature T, determined using Eq. (8) at various beam energies, are listed in the Table I. As discussed earlier, in the present reactions both 0n and 1n channels contribute in the α-particle kinetic energy region of interest, therefore, the $\bar{K}$ values determined through the ^{16}O + ^{94}Mo and ^{16}O + ^{100}Mo reactions correspond respectively to ^{105,106}Cd and ^{111,112}Cd residual nuclei.

Nuclear temperatures were also estimated from Maxwellian fitting of the α-evaporation spectra at each beam energy using the following functional form [49]:

$$\frac{d^2\sigma}{d\Omega dE} = \frac{N}{T^2}(E_\alpha - E_b)\exp\left[-(E_\alpha - E_b)/T\right], \tag{9}$$

where N, E_b, and T are the normalization constant, emission barrier, and slope (temperature) of the spectra, respectively. The Maxwellian fitted nuclear temperature are provided in the Table I for both the nuclear systems. It is seen that Maxwellian fitted nuclear temperatures are consistently somewhat higher than those obtained from the statistical model analysis (PACE2 code).

The best fit inverse level-density parameter $\bar{K}$ is plotted as a function of nuclear temperature in Fig. 10 for both the compound nuclear systems; ^{110}Sn* and ^{116}Sn*. It is observed that the inverse level-density parameter, K, increases for both the systems with increasing temperature up to 1.8 MeV and after that, it slowly saturates. It is observed that in the temperature region below 1.8 MeV, the parameter K is higher for neutron-rich ^{116}Sn* by around 1 MeV in comparison to the neutron deficient ^{110}Sn*. The high K value for neutron-rich nucleus as seen above may directly be linked with isospin of the respective nuclei. These experimental results of isospin dependence of parameter K show good agreement with Quraishi *et al.* [23] calculations in which they have conjectured that nuclear level-density parameter, a, is lower for neutron-rich nuclei.

TABLE I. Experimental parameters of nuclear reactions studied and results obtained from the present work.

	^{16}O+^{94}Mo					^{16}O+^{100}Mo				
Beam energy (MeV)	E_{ex}^{CN}[a] (MeV)	$\bar{K}$ (MeV)	$\bar{E}_X$ (MeV)	T(MeV) from Eq. (8)	T(MeV) Maxwellian fit	E_{ex}^{CN}[a] (MeV)	$\bar{K}$ (MeV)	$\bar{E}_X$ (MeV)	T(MeV) from Eq. (8)	T(MeV) Maxwellian fit
55.0	38.0	8.7±0.1	14.4	1.15	1.19±0.02	46.4	9.7±0.2	18.3	1.24	1.39±0.02
60.0	42.4	9.1±0.1	17.1	1.24	1.33±0.01	50.7	9.8±0.1	21.0	1.32	1.50±0.01
70.0	51.0	9.5±0.1	24.0	1.45	1.57±0.02	59.5	10.5±0.2	25.1	1.43	1.77±0.02
75.0	55.7	9.8±0.1	28.0	1.55	1.71±0.02	63.8	10.8±0.1	29.3	1.54	1.83±0.02
80.0	59.7	9.8±0.2	30.0	1.61	1.75±0.03	68.2	11.0±0.1	32.3	1.61	1.98±0.01
95.5						81.7	10.9±0.2	42.8	1.84	2.28±0.02
104.9						89.1	11.1±0.1	46.4	1.91	2.41±0.02
114.6						98.3	10.9±0.1	52.0	2.02	2.55±0.02
124.6						107.0	11.3±0.2	56.6	2.10	2.72±0.02
136.6						117.4	11.4±0.3	62.9	2.21	2.90±0.03
		10.8[b]					11.2[b]			

[a]Compound nucleus excitation energy after correcting for energy loss in the target.
[b]RMF calculations [24].

Earlier, self-consistent calculations were carried out by Nerlo-Pomorska *et al*. [24] for excited nuclei in the framework of the relativistic mean-field theory at temperatures between 0 and 4 MeV for several spherical even-even nuclei. In their work, the temperature-dependent macroscopic part of the thermal energy was approximated by a liquid-drop type formula. Thus, a global parametrization was obtained for the liquid-drop type level-density parameter, which, within this formalism is constant in the temperature region between 0 and 4 MeV. Using those global parameters, a liquid-drop inverse level-density parameter (K_{LD}) was calculated for several Cd isotopes. It is seen that the K_{LD} parameter also increases with neutron richness as observed in the present work. The K_{LD} values for ^{106}Cd (^{16}O + ^{94}Mo reaction) and ^{112}Cd (^{16}O + ^{100}Mo reaction) are calculated to be 10.8 MeV and 11.2 MeV, respectively. These K_{LD} values are also provided in the Table I.

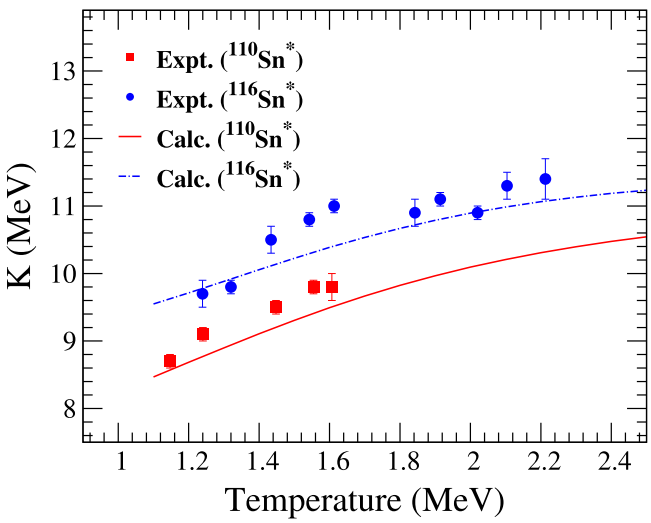

FIG. 10. Inverse level-density parameter as a function of temperature (see text). The experimental data (symbols) are compared with semiclassical model predictions; dash-dotted and solid lines represent ^{116}Sn* and ^{110}Sn* compound nuclei, respectively.

It is worth discussing theoretical work of Arunachalam *et al*. [50], where nuclear level-density is calculated as a function of nuclear temperature for various isospin values. It has been shown that level-density parameter vary quite dramatically below nuclear temperature around 1.5 MeV in the mass region of $A \approx 90$. Depending on the total isospin, level-density parameter increases or decreases with increasing temperature up to around 1.5 MeV. At higher temperatures (beyond around 1.5 MeV) the level-density parameter saturates. It is clearly shown in the work of Arunachalam *et al*. [50] that the saturated value of the level-density parameter is lower for the higher isospin values which is consistent with the present work and the conjuncture of Quraishi *et al*. [23]. It would be of further interest to have more measurements on nuclear level-density parameter in the temperature region around 1 MeV in different isotopic chains.

V. COMPARISON WITH CALCULATIONS USING SEMICLASSICAL TRACE FORMULA

Semiclassical trace formula for single-particle level-density $[g(E) = \tilde{g}(E) + \delta g(E)]$ for two- and three-dimensional harmonic oscillator potentials using periodic-orbit theory have been derived in Ref. [51]. The average part of level-density $\tilde{g}(E)$ for the harmonic oscillator potential with

$$\hbar\omega_x = p\,\hbar\omega_0^*, \quad \hbar\omega_y = p\,\hbar\omega_0^*, \text{ and } \hbar\omega_z = n'\hbar\omega_0^*, \qquad (10)$$

where p is an integer and n' is an irrational number, is given as:

$$\tilde{g}(E) = \frac{1}{2n'\hbar\omega_0^{*3}}\left[E^2 - \frac{1}{12}\left(2\hbar\omega_0^{*2} + n'^2\hbar\omega_0^{*2}\right)\right]. \qquad (11)$$

Following the methodology as described in Refs. [25,52], we can find the partition function $Z(\beta)$ as its Laplace transform and, subsequently, the finite-temperature partition function is

given as:

$$Z_T(\beta) = Z(\beta)\frac{\pi\beta T}{\sin(\pi\beta T)}. \tag{12}$$

Here β is just a variable which can be of complex nature, too. Taking the inverse Laplace transform of Eq. (12), we have found the temperature-dependent single-particle level-density as follows:

$$\tilde{g}_T(E) = \frac{1}{2p^2n'(\hbar\omega_0^*)^3}\left\{E^2 + \frac{\pi^2T^3}{3} - \frac{(2p^2+n'^2)}{12}(\hbar\omega_0^*)^2 \times \left[\frac{\exp(E/T)}{1+\exp(E/T)}\right]\right\}. \tag{13}$$

Here $\hbar\omega_0^*$ is deformation dependent oscillator strength, and, for a nucleus with mass number A, atomic number Z, and neutron number N, it is given as:

$$\hbar\omega_0^{n,p} = \frac{41}{A^{1/3}}\left(1 \pm \frac{N-Z}{A}\right)^{1/3} \text{MeV}.$$

Superscripts $\{n, p\}$ describe that while performing the calculations, we have kept neutrons and protons on different footings. δ is the deformation parameter which is related to the quadruple deformation parameter $\delta \sim 0.95\,\beta_2$. The oscillator frequencies in terms of deformation parameter δ can be written as:

$$\hbar\omega_x^{n,p} = \hbar\omega_y^{n,p} = \hbar\omega_\perp^{n,p} = \hbar\omega_0^{*n,p}\left(1+\frac{\delta}{3}\right)$$
$$\hbar\omega_z^{n,p} = \hbar\omega_0^{*n,p}\left(1-\frac{2\delta}{3}\right). \tag{14}$$

So the deformation parameter is given as [53]:

$$\delta = \frac{\hbar\omega_\perp - \hbar\omega_z}{\hbar\omega_0^*}. \tag{15}$$

If we choose $p = 1$, then the oscillatory part of the level-density is given as [51]:

$$\delta g(E) = \frac{E}{\hbar\omega_0^{*2}}\sum_{k=1}^{\infty}\frac{1}{\sin(k\pi n')}\sin\left(\frac{2k\pi E}{\hbar\omega_0^*}\right) + \frac{n'}{2\hbar\omega_0^*}\sum_{k=1}^{\infty}\frac{\cos(k\pi n')}{\sin^2(k\pi n')}\cos\left(\frac{2k\pi E}{\hbar\omega_0^*}\right) + \frac{1}{2n'\hbar\omega_0^*}\sum_{k=1}^{\infty}\frac{(-1)^{k+1}}{\sin^2\left(\frac{k\pi}{n'}\right)}\cos\left(\frac{2k\pi E}{\hbar\omega_0^*}\right). \tag{16}$$

We develop temperature-dependent expression for level-density following the methodology described in Refs. [25,52] as given below:

$$\delta g_T(E) = \sum_{k=1}^{\infty}\frac{\tau\left[E\sin\left(\frac{2k\pi E}{\hbar\omega_0^*}\right) + \left(\pi T\coth\tau - \frac{\hbar\omega_0}{k\pi}\right)\cos\left(\frac{2k\pi E}{\hbar\omega_0^*}\right)\right]}{(\hbar\omega_0^*)^2\sin(k\pi n')\sinh\tau} + \sum_{k=1}^{\infty}\frac{\tau n'}{2\hbar\omega_0^*}\frac{\cot(k\pi n')\cos\left(\frac{2k\pi E}{\hbar\omega_0^*}\right)}{\sin(k\pi n')\sinh\tau} + \sum_{k=1}^{\infty}\frac{(-1)^{k+1}}{2}\frac{\tau\cos\left(\frac{2k\pi E}{\hbar\omega_0^*}\right)}{n'^2\hbar\omega_0^*\sin^2\left(\frac{k\pi}{n'}\right)\sinh\left(\frac{\tau}{n'}\right)} + \sum_{s=1}^{\infty}\sum_{k=1}^{\infty}\frac{4k\pi(-1)^s\left(\frac{s}{T}\right)^2\exp(-sE/T)}{(\hbar\omega_0^*)^3\left[\left(\frac{s}{T}\right)^2+\left(\frac{2k\pi}{\hbar\omega_0^*}\right)^2\right]^2} + \sum_{s=1}^{\infty}\sum_{k=1}^{\infty}\frac{(-1)^s n'\cos(k\pi n')(s/T)^2\exp(-sE/T)}{2\hbar\omega_0^*\sin^2(k\pi n')\left[\left(\frac{s}{T}\right)^2+\left(\frac{2k\pi}{\hbar\omega_0^*}\right)^2\right]} + \sum_{s=1}^{\infty}\sum_{k=1}^{\infty}\frac{(-1)^{k+s}(s/T)^3\exp(-sE/T)}{2n'\hbar\omega_0^*\sin\left(\frac{k\pi}{n'}\right)\left[\left(\frac{s}{T}\right)^2+\left(\frac{2k\pi}{n'\hbar\omega_0^*}\right)^2\right]}. \tag{17}$$

Here $\tau = \frac{2\pi^2kT}{\hbar\omega_0^*}$ and T is the nuclear temperature. The total expression is now given as:

$$g_T(E) = \tilde{g}_T(E) + \delta g_T(E). \tag{18}$$

The level-density parameter [48]

$$a_T = \sum_{n,p}\frac{\pi^2}{6}g_T(\mu^{n,p}), \tag{19}$$

where $\mu^{n,p}$ is the chemical potential and it is fixed by the following relation:

$$N, Z = \int_0^{\mu^{n,p}} g_T(E)dE. \tag{20}$$

Present calculations are carried out for ^{106}Cd and ^{112}Cd nuclei by assuming first chance α-particle emission. The deformation parameter δ is taken as 0.156 and $\hbar\omega_0^{*n,p}$ is taken as 1.21 $\hbar\omega_0^{n,p}$ while the repetitions over periodic orbits (k) are from 1 to 5 and the sum over s is taken from 1 to 4 for ^{106}Cd nucleus. However, for ^{112}Cd isotope, we have used $\delta = 0.162$ while the sums over k and s are taken by varying them from 1 to 5. $\hbar\omega_0^{*n,p}$ is taken as 1.26 $\hbar\omega_0^{n,p}$ in case of ^{112}Cd. Now, we can determine temperature-dependent level-density parameter using Eq. (20).

The calculated a_T values as a function of nuclear temperature were converted for inverse level-density parameter, K_T, using $K_T = A/a_T$. The inverse level-density parameter K_T, thus calculated using the semiclassical approach, was compared with those determined from statistical model analysis of the α-particle evaporation spectra as shown in the Fig. 10 for both the nuclear systems. It is observed that semiclassical calculations reproduce the increasing trend of inverse level-density parameter with temperature reasonably well for both the nuclear systems. Semiclassical calculations also predict that difference in the calculated K values for both the isotopes decreases with increasing temperature(see Fig. 10).

VI. SUMMARY

α-Particle evaporation spectra from ^{110}Sn* and ^{116}Sn* compound nuclei have been measured. These compound nuclei were populated employing ^{16}O + ^{94,100}Mo reactions at varying beam energies in the range of 55 to 136 MeV using BARC-TIFR Pelletron Linac facility. Statistical model

analysis of experimental data was carried out using PACE2 code to determine the level-density parameter as a function of temperature for the two residual nuclei (^{106}Cd and ^{112}Cd) having significantly different isospins. It is observed that the inverse level-density parameter, K, initially increases with temperature for both systems up to 1.8 MeV, and thereafter, it gradually saturates. Semiclassical calculations including isospin effects reproduced the K values as obtained from the statistical model analysis of α-particle evaporation spectra. Present observation of increasing K values with nuclear temperature is consistent with the predictions of microscopic theory proposed earlier by Shalomo *et al*. [8]. It is also observed that the level-density parameter is lower for the neutron-rich isotope in the temperature region below 1.8 MeV. This observation, in turn, support finite dependence of nuclear level-density parameter on isospin as conjectured earlier by Quraishi *et al*. [22]. Nevertheless, it will be stimulating to carry out further measurements on nuclear level-density parameter to explore its evolution with nuclear isospin in different mass pockets of the nuclear chart.

ACKNOWLEDGMENTS

Authors thank the operating staff of Pelletron/Linac accelerator facility for excellent operation of the machine. The authors also acknowledge R. P. Vind, A. L. Inkar, R.V Jangale, and L. A. Kinage for their help during the experiment.

[1] H. A. Bethe, Phys. Rev. **50**, 332 (1936).
[2] A. Gilbert and A. G. W. Cameron, Can. J. Phys. **43**, 1446 (1965).
[3] R. Stokstad, *Treatise on Heavy Ion Science*, Vol. 3, edited by D. A. Bromley (Plenum, New York, 1985), p. 83.
[4] A. Iljinov, M. Mebel, N. Bianchi, E. D. Sanctis, C. Guaraldo, V. Lucherini, V. Muccifora, E. Polli, A. Reolon, and P. Rossi, Nucl. Phys. A **543**, 517 (1992).
[5] A. V. Ignatyuk, G. N. Smirenkin, and A. S. Tishin, Sov. J. Nucl. Phys. **21**, 255 (1975).
[6] R. J. Charity, L. G. Sobotka, J. F. Dempsey *et al.*, Phys. Rev. C **67**, 044611 (2003).
[7] R. J. Charity, Phys. Rev. C **82**, 014610 (2010).
[8] S. Shlomo and J. Natowitz, Phys. Lett. B **252**, 187 (1990).
[9] G. Nebbia, K. Hagel, D. Fabris *et al.*, Phys. Lett. B **176**, 20 (1986).
[10] D. Fabris, E. Fioretto, G. Viesti *et al.*, Phys. Rev. C **50**, R1261 (1994).
[11] M. Gonin, L. Cooke, K. Hagel *et al.*, Phys. Lett. B **217**, 406 (1989).
[12] M. Gonin, L. Cooke, K. Hagel *et al.*, Phys. Rev. C **42**, 2125 (1990).
[13] K. Hagel, D. Fabris, P. Gonthier *et al.*, Nucl. Phys. A **486**, 429 (1988).
[14] P. Roy, K. Banerjee, C. Bhattacharya *et al.*, Phys. Rev. C **94**, 064607 (2016).
[15] R. Hasse and P. Schuck, Phys. Lett. B **179**, 313 (1986).
[16] S. Shlomo and J. B. Natowitz, Phys. Rev. C **44**, 2878 (1991).
[17] J. B. Natowitz, R. Wada, K. Hagel, T. Keutgen, M. Murray, A. Makeev, L. Qin, P. Smith, and C. Hamilton, Phys. Rev. C **65**, 034618 (2002).
[18] J. B. Natowitz, K. Hagel, Y. Ma, M. Murray, L. Qin, R. Wada, and J. Wang, Phys. Rev. Lett. **89**, 212701 (2002).
[19] B. Borderie and M. F. Rivet, Prog. Part. Nucl. Phys **61**, 551 (2008).
[20] A. Brondi, A. Di Nitto, G. La Rana *et al.*, Euro. Phys. J: Conf. Ser. **2**, 04002 (2010).
[21] A. Di Nitto, A. Brondi, G. La Rana, R. Moro, P. N. Nadtochy, E. Vardaci, N. Gelli, M. Cinausero, and G. Prete, J. Phys.: Conf. Ser. **267**, 012053 (2011).
[22] S. I. Al-Quraishi, S. M. Grimes, T. N. Massey, and D. A. Resler, Phys. Rev. C **67**, 015803 (2003).
[23] S. I. Al-Quraishi, S. M. Grimes, T. N. Massey, and D. A. Resler, Phys. Rev. C **63**, 065803 (2001).
[24] B. Nerlo-Pomorska, K. Pomorski, J. Bartel, and K. Dietrich, Phys. Rev. C **66**, 051302(R) (2002).
[25] H. Kaur and S. R. Jain, J. Phys. G: Nucl. Part. Phys. **42**, 115103 (2015).
[26] B. V. Zhuravlev, A. A. Lychagin, and N. N. Titarenko, Phys. At. Nucl. **69**, 363 (2006).
[27] P. Marini, M. F. Rivet, B. Borderie, N. Le Neindre, A. Chbihi, G. Verde, and J. Wieleczko, Euro. Phys. J: Conf. Ser. **2**, 04003 (2010).
[28] I. M. Govil, J. Huizenga, W. U. Schröder, and J. Töke, Phys. Lett. B **197**, 515 (1987).
[29] J. Gomez del Campo, D. Shapira, M. Korolija *et al.*, Phys. Rev. C **53**, 222 (1996).
[30] D. R. Chakrabarty, V. M. Datar, S. Kumar, E. T. Mirgule, H. H. Oza, and U. K. Pal, Phys. Rev. C **51**, 2942 (1995).
[31] B. John, S. K. Kataria, B. S. Tomar, A. Goswami, G. K. Gubbi, and S. B. Manohar, Phys. Rev. C **56**, 2582 (1997).
[32] B. John, R. K. Choudhury, B. K. Nayak, A. Saxena, and D. C. Biswas, Phys. Rev. C **63**, 054301 (2001).
[33] Y. K. Gupta, B. John, D. C. Biswas, B. K. Nayak, A. Saxena, and R. K. Choudhury, Phys. Rev. C **78**, 054609 (2008).
[34] Y. K. Gupta, D. C. Biswas, B. John, B. K. Nayak, A. Saxena, and R. K. Choudhury, Phys. Rev. C **80**, 054611 (2009).
[35] A. Gavron, Phys. Rev. C **21**, 230 (1980).
[36] Y. K. Gupta, D. C. Biswas, P. Roy, B. K. Nayak, R. G. Thomas, A. L. Inkar, R. P. Vind, B. John, A. Saxena, and R. K. Choudhury, Nucl. Instrum. Methods A **629**, 149 (2011).
[37] Y. K. Gupta, G. K. Prajapati, L. S. Danu, B. N. Joshi, A. L. Inkar, R. Jangale, R. P. Vind, S. Mukhopadhyay, B. John, and D. C. Biswas, Nucl. Instrum. Methods A **947**, 162750 (2019).
[38] B. John, S. S. Kumar, M. Kumar, R. V. Jangale, A. L. Inkar, and L. Kinage, J. Phys.: Conf. Ser. **390**, 012042 (2012).
[39] Y. K. Gupta, D. C. Biswas, B. John, B. K. Nayak, A. Chatterjee, and R. K. Choudhury, Phys. Rev. C **86**, 014615 (2012).
[40] Y. K. Gupta, D. C. Biswas, G. K. Prajapati, L. S. Danu, B. N. Joshi, S. Mukhopadhyay, B. V. John, S. Dubey, S. Chettri, N. Kumar, R. P. Vind, and S. Mukherjee, Phys. Rev. C **98**, 041601(R) (2018).
[41] J. Gál, G. Kalinka, B. M. Nyakó, G. E. Perez, Z. Máté, G. Hegyesi, T. Vass, A. Kerek, and A. Johnson, Nucl. Instrum. Methods A **366**, 120 (1995).
[42] A. Jhingan, P. Sugathan, G. Kaur, K. Kapoor, N. Saneesh, T. Banerjee, H. Singh, A. Kumar, B. R. Behera, and B. K. Nayak, Nucl. Instrum. Methods A **786**, 51 (2015).

[43] R. Bass, Phys. Rev. Lett. **39**, 265 (1977).
[44] A. J. Sierk, Phys. Rev. C **33**, 2039 (1986).
[45] P. Moller, J. R. Nix, W. D. Myers, and W. J. Swiatecki, At. Data Nucl. Data Tables **59**, 185 (1995).
[46] J. Huizenga and G. Igo, Nucl. Phys. **29**, 462 (1962).
[47] D. Cline and P. Lesser, Nucl. Instrum. Methods **82**, 291 (1970).
[48] A. Bohr and B. R. Mottelson, *Nuclear Structure* (World Scientific, Singapore, 1998).
[49] G. Nebbia, D. Fabris, A. Perin *et al.*, Nucl. Phys. A **578**, 285 (1994).
[50] N. Arunachalam, A. Mohamed Akbar, S. Veeraraghavan, and M. Rajasekaran, Phys. Rev. C **45**, 1667 (1992).
[51] M. Brack and S. R. Jain, Phys. Rev. A **51**, 3462 (1995).
[52] M. Brack and R. K. Bhaduri, *Semiclassical Physics*, Frontiers in Physics (Westview Press, Boulder, CO, 2003).
[53] I. Ragnarsson and S. G. Nilsson, *Shapes and Shells in Nuclear Structure* (Cambridge University Press, Cambridge, UK, 1995).